

High-pressure and high-temperature sintering of pure cubic silicon carbide: A study on stress-strain and densification

Jin-Xin Liu(刘金鑫), Fang Peng(彭放), Guo-Long Ma(马国龙), Wen-Jia Liang(梁文嘉), Rui-Qi He(何瑞琦), Shi-Xue Guan(管诗雪), Yue Tang(唐越), and Xiao-Jun Xiang(向晓君)

Citation: Chin. Phys. B, 2023, 32 (**9**): 098101. DOI: 10.1088/1674-1056/aca6d4
Journal homepage: http://cpb.iphy.ac.cn; http://iopscience.iop.org/cpb

What follows is a list of articles you may be interested in

Synergistic influences of titanium, boron, and oxygen on large-size single-crystal diamond growth at high pressure and high temperature

Guang-Tong Zhou(周广通), Yu-Hu Mu(穆玉虎), Yuan-Wen Song(宋元文), Zhuang-Fei Zhang(张壮飞), Yue-Wen Zhang(张跃文), Wei-Xia Shen(沈维霞), Qian-Qian Wang(王倩倩), Biao Wan(万彪), Chao Fang(房超), Liang-Chao Chen(陈良超), Ya-Dong Li(李亚东), and Xiao-Peng Jia(贾晓鹏)

Chin. Phys. B, 2022, 31 (**6**): 068103. DOI: 10.1088/1674-1056/ac4650

Synthesis and characterizations of boron and nitrogen co-doped high pressure and high temperature large single-crystal diamonds with increased mobility

Xin-Yuan Miao(苗辛原), Hong-An Ma(马红安), Zhuang-Fei Zhang(张壮飞), Liang-Chao Chen(陈良超), Li-Juan Zhou(周丽娟), Min-Si Li(李敏斯), and Xiao-Peng Jia(贾晓鹏)

Chin. Phys. B, 2021, 30 (**6**): 068102. DOI: 10.1088/1674-1056/abf12c

Crystallization and characteristics of {100}-oriented diamond with CH_4N_2S additive under high pressure and high temperature

Yong Li(李勇), Debing Tan(谭德斌), Qiang Wang(王强), Zhengguo Xiao(肖政国), Changhai Tian(田昌海), Lin Chen(陈琳)

Chin. Phys. B, 2020, 29 (**9**): 098103. DOI: 10.1088/1674-1056/ab99b9

Regulation mechanism of catalyst structure on diamond crystal morphology under HPHT process

Ya-Dong Li(李亚东), Yong-Shan Cheng(程永珊), Meng-Jie Su(宿梦洁), Qi-Fu Ran(冉启甫), Chun-Xiao Wang(王春晓), Hong-An Ma(马红安), Chao Fang(房超), Liang-Chao Chen(陈良超)

Chin. Phys. B, 2020, 29 (**7**): 078101. DOI: 10.1088/1674-1056/ab90e8

Characteristics of urea under high pressure and high temperature

Shuai Fang(房帅), Hong-An Ma(马红安), Long-Suo Guo(郭龙锁), Liang-Chao Chen(陈良超), Yao Wang(王遥), Lu-Yao Ding(丁路遥), Zheng-Hao Cai(蔡正浩), Jian Wang(王健), Xiao-Peng Jia(贾晓鹏)

Chin. Phys. B, 2019, 28 (**9**): 098101. DOI: 10.1088/1674-1056/ab3445

High-pressure and high-temperature sintering of pure cubic silicon carbide: A study on stress–strain and densification

Jin-Xin Liu(刘金鑫), Fang Peng(彭放)†, Guo-Long Ma(马国龙), Wen-Jia Liang(梁文嘉), Rui-Qi He(何瑞琦), Shi-Xue Guan(管诗雪), Yue Tang(唐越), and Xiao-Jun Xiang(向晓君)

Institute of Atomic and Molecular Physics, Sichuan University, Chengdu 610065, *China*

(Received 19 August 2022; revised manuscript received 7 November 2022; accepted manuscript online 29 November 2022)

Silicon carbide (SiC) is a high-performance structural ceramic material with excellent comprehensive properties, and is unmatched by metals and other structural materials. In this paper, raw SiC powder with an average grain size of 5 μm was sintered by an isothermal-compression process at 5.0 GPa and 1500 °C; the maximum hardness of the sintered samples was 31.3 GPa. Subsequently, scanning electron microscopy was used to observe the microscopic morphology of the recovered SiC samples treated in a temperature and extended pressure range of 0–1500 °C and 0–16.0 GPa, respectively. Defects and plastic deformation in the SiC grains were further analyzed by transmission electron microscopy. Further, high-pressure *in situ* synchrotron radiation x-ray diffraction was used to study the intergranular stress distribution and yield strength under non-hydrostatic compression. This study provides a new viewpoint for the sintering of pure phase micron-sized SiC particles.

Keywords: high pressure and high temperature, silicon carbide, stress analysis, defect

PACS: 81.20.Ev, 61.72.Ff, 81.05.Je **DOI:** 10.1088/1674-1056/aca6d4

1. Introduction

Silicon carbide (SiC) has excellent high-temperature mechanical capabilities due to its high degree of covalent bonding and stable crystal structure, which also contribute to its high hardness, high elastic modulus, and superior wear resistance. Additionally, it possesses good thermal conductivity, oxidation resistance, and corrosion resistance. These outstanding properties enable SiC to be used in a wide range of applications, not only in traditional industrial fields, but also in high-technology fields, such as nuclear energy, space technology, and semiconductors.[1–4]

Therefore, the issue of obtaining high-quality SiC polycrystalline ceramics by sintering SiC powder has always been a focus of attention. Commonly used technologies for SiC block processing include hot pressing, pressureless sintering, spark-plasma sintering, and hot isostatic pressing using commercial powder raw materials.[5]

Unfortunately, because SiC possesses strong covalent bonds, a low self-diffusion coefficient, and a low volume-diffusion rate, realizing the sintering process of SiC is challenging.[6] In order to solve this issue, additives can be used for sintering; however, the presence of additives will affect the microstructure and properties of the bulk materials formed after sintering.[6–9] In addition, due to a lack of sufficient external driving force, the use of traditional sintering technology is also difficult. Polycrystalline SiC consolidated by these methods shows a coarse-grained microstructure because higher processing temperatures are applied over a longer period of time.[5]

The difference is that, in a high-pressure and high-temperature (HPHT) sintering process, high pressure can inhibit grain coarsening, while a high temperature can promote grain coalescence and the generation of strong interfaces.[10–13] Sun *et al.* sintered β-SiC without a binder at 25 GPa and 1400 °C, and the hardness of the sintered body reached more than 40 GPa.[10] Matovic *et al.* studied the high-pressure sintering of β-SiC nanoparticles.[11] High values of nano-hardness (32 GPa) and elastic modulus (420 GPa) could be obtained by applying a high pressure of 4 GPa at 1500 °C. Matović *et al.* sintered cubic silicon carbide nanoparticles without sintering additives under high temperature and high pressure, and the relative density of the sintered samples reached 99%.[14]

In addition, the process of polycrystalline structure formation in HPHT sintering methods is very complex and is related to the properties and purity of the initial powder, as well as pressure and temperature parameters.[15] Under cold-pressing conditions, the initial rearrangement is caused by the mutual slip of the grains when pressure is applied to the crystal, and the mutual extrusion of the grains leads to crushing.[12,16–23] The plastic deformation of grains and the formation of polycrystalline structures are often influenced by the pressure and temperature treatment.[24–29] However, there is a lack of research on the cold-pressing stage and sintering process of SiC sintered by the HPHT method, and these critical issues require further research in order to be elucidated.

†Corresponding author. E-mail: pengfang@scu.edu.cn

© 2023 Chinese Physical Society and IOP Publishing Ltd

Studying the brittle fracture, stress distribution, and plastic deformation of SiC powder in the cold-pressing stage is of great significance for understanding the isothermal compression (increasing pressure with a constant sample chamber temperature) sintering mechanism of polycrystalline SiC. In this paper, we obtain the fracture characteristics and mechanism of micron-sized cubic SiC particles with and without temperature under different pressures. The defects and crushing behavior of SiC powder during sintering are investigated by transmission electron microscopy (TEM) and scanning electron microscopy (SEM). Furthermore, the stress and yield strength in the SiC powder are measured *in situ* under high pressure by synchrotron radiation x-ray diffraction techniques and the data are analyzed. This work is useful for improving understanding, and will guide the sintering of high-quality pure phase polycrystalline SiC.

2. Experimental procedures and methods

2.1. High-pressure and high-temperature treatment

The experimental samples were made using SiC (face-centered cubic zinc blend structure) powder with an initial average grain size of about 5 μm. A certain quality of SiC powder was assembled into a cubic pyrophyllite pressure-transmitting medium, used for a cold-pressing crushing and was sintered in a two-part experiment. Pressures below 5.5 GPa were provided by a DS 6×14 MN cubic press and the higher pressures were provided by a DS 6×8 MN cubic press. The pressure was calibrated at ambient temperature using known phase transitions of Bi, Tl, and ZnS.[30] For the cold-pressing experiment, the SiC powder was compressed to the set pressure and held for 10 min, then the pressure was reduced to an ambient pressure and recovered for subsequent characterization. The SiC samples were sintered in a cubic press chamber under different temperature and pressure conditions and exposed isothermally for 10 min at a given temperature.

2.2. Characterization

X-ray diffraction (XRD) patterns of the starting powder and samples treated by HPHT were tested on an x-ray diffractometer (DX-2700BH, China) with a Cu-$K\alpha$ radiation source (λ = 1.5404 Å). The morphology and microstructure of the fragmented grains of the recovered samples were characterized by SEM (JSM-IT500HR, Japan) measurements with an accelerating voltage of 0.5–30 kV. The microdefects of the polycrystalline SiC samples were studied by TEM (JEM-2100PLUS, Japan). The Vickers hardness of the end-polished samples was tested using a Vickers hardness tester (FV-700B, Future-Tech, Japan). The density of the sample was tested on a density balance (MP3002, China).

2.3. High-pressure *in situ* synchrotron radiation experiment

High-pressure *in situ* synchrotron radiation x-ray diffraction was conducted at the 4W2 beamline at the Beijing Synchrotron Radiation Facility (BSRF, China). The spot size of the incident synchrotron radiation x-ray beam was $\sim 36 \times 15$ μm^2, with a wavelength of 0.6199 Å. The SiC powder was loaded into the sample chamber of a diamond anvil cell (DAC) with a T301 stainless steel sheet as the gasket material, and no pressure transmitting medium was used. The gasket was pre-indented to a thickness of 20 μm and a 100 μm hole drilled in the T301 gasket served as a sample chamber. A small ruby ball was placed on top of the sample as a pressure standard. Two-dimensional diffraction patterns were collected by a CCD imaging plate detector, and the two-dimensional diffraction rings were then integrated into one-dimensional images by the FIT2D software package for subsequent analysis and processing.

3. Results and discussion

3.1. Effect of temperature on SiC sintered bulk

The recovered SiC samples sintered at a pressure of 5.0 GPa and different temperatures were characterized by SEM. In Fig. 1(b), at 300 °C, the surface cracks tend to close, but the change in particle size is not obvious. In Fig. 1(c), it can be seen that, at 600 °C, there are almost no cracks on the surface of the particles, and creep between particles begins to appear. Figure 1(d) shows that adhesion creep occurs in most grains at 900 °C. In Fig. 1(e), at 1100 °C, the void is obviously reduced and the grain boundary is blurred. In Fig. 1(f), the grain boundary at 1300 °C is difficult to distinguish, and the densification increases. The gradual closing of the surface cracks of the particles, the grain boundary creep, the porosity decrease, and the densification increase are all a result of temperature effects. The plastic-deformation mechanism of SiC is what causes the change in grain shape as the sintering temperature rises. Thus, crack closure and the formation of new atomic bonds for the plastic deformation of SiC ceramic materials occur.

Figure 2(a) shows XRD patterns of the SiC samples sintered at different temperatures at a pressure of 5.0 GPa. The main XRD peaks for the sintered samples can be indexed to the zinc blend-structured SiC. The weak peak at $2\theta = 33.6°$ in the XRD pattern of the sample can be attributed to the stacking faults of the (111) planes in cubic SiC.[10] This indicates that SiC does not undergo phase transformation and decomposition at the available temperatures and pressures.[31,32] In Fig. 2(b), the full width at half-maximum (FWHM) of the diffraction peak tends to widen first and then narrow with increasing temperature. The FWHM is influenced by grain size

and stress.[33,34] There is mechanical bonding between grains at low temperatures. Following decompression, a significant amount of the local strain generated at high pressure is released. The FWHM of the diffraction peak is lower. The surface cracks of the granules gradually close as the temperature rises, and even when the pressure is removed, some of the stress is still present inside the grain. The periodic arrangement of the crystal is shown by the XRD peak of the grain. The widening of the FWHM is also related to the existence of microscopic deviatoric strain.

The FWHM of the diffraction peak at 5.0 GPa cold pressing changes as a result of the crystal lattice distortion. The lattice is further distorted, the stress increases, and the FWHM broadens under the induction of temperature. The FWHMs of the diffraction peaks widen. Finally, the FWHM narrows as the high temperature promotes stress relaxation.

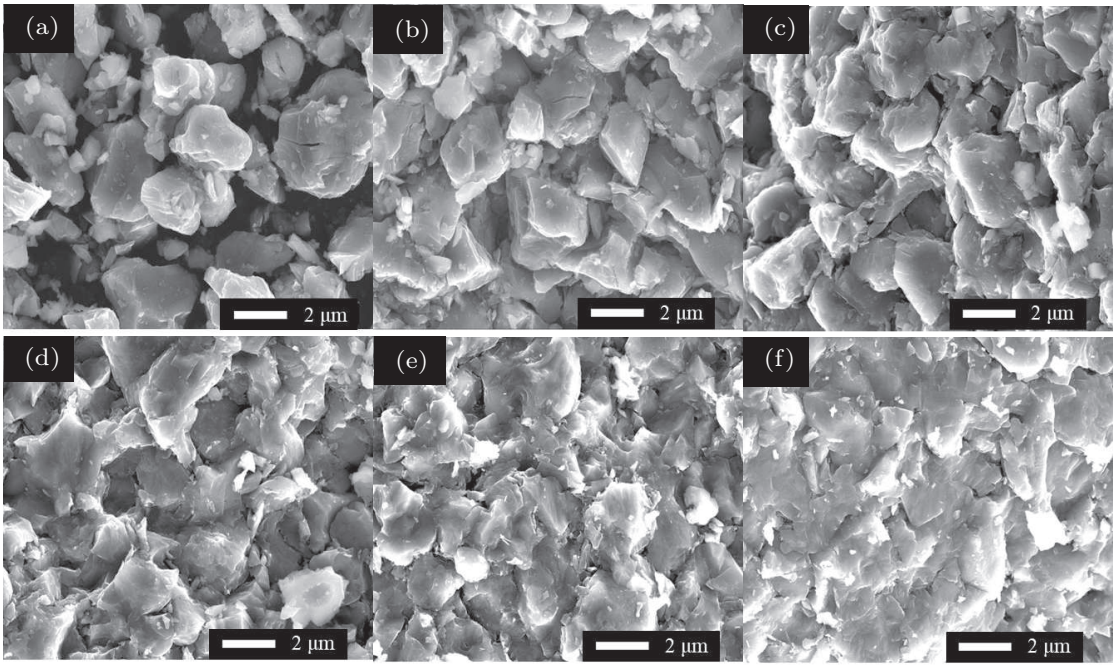


Fig. 1. SEM images of SiC sintered at 5.0 GPa pressure and different temperatures. (a) Ambient temperature; (b) 300 °C; (c) 600 °C; (d) 900 °C; (e) 1100 °C; and (f) 1300 °C.

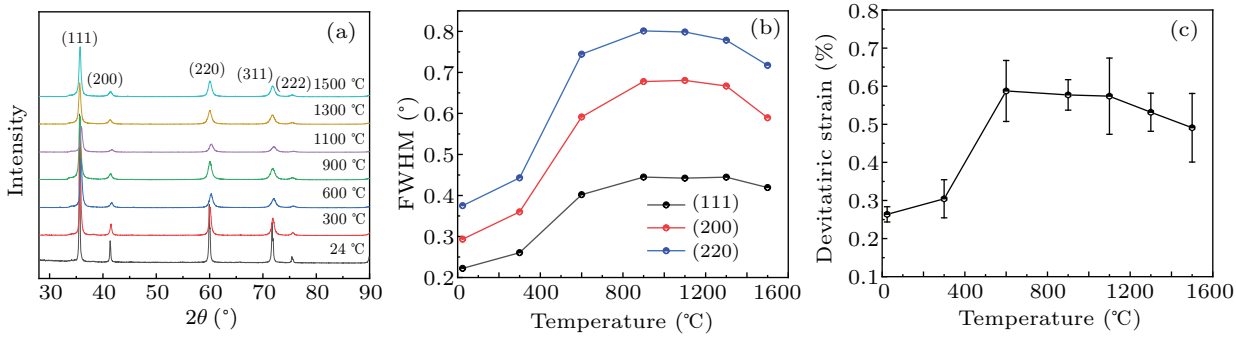


Fig. 2. (a) XRD patterns at 5.0 GPa and different temperatures. (b) Change of the full width at half-maximum of the different crystal planes of the SiC sintered body with the sintering temperature. (c) Variation of the deviatoric strain of the SiC sintered body with the sintering temperature.

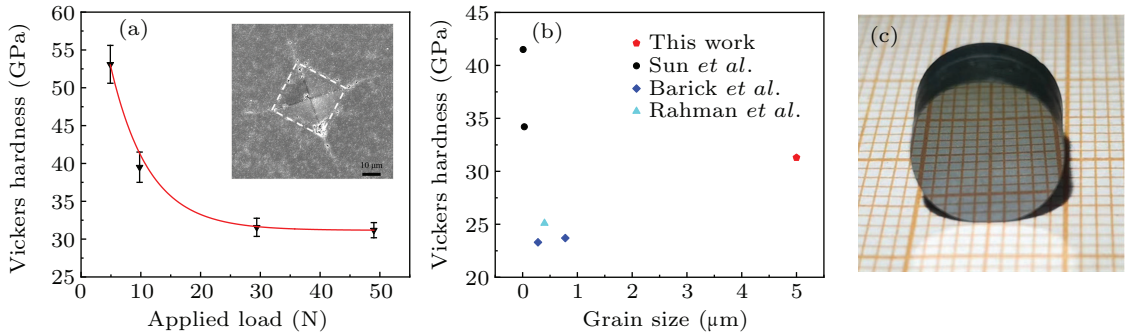


Fig. 3. (a) Vickers hardness of SiC samples sintered at 5.0 GPa and 1500 °C vs. the loading force. Inset: SEM image of Vickers indentation under a 29.4 N loading force. (b) Relation between the Vickers hardness and the grain size of SiC bulks. (c) Optical photographs of the end-polished SiC sample.

Furthermore, Fig. 3 shows the hardness and optical photographs of the SiC sintered bulk at 5.0 GPa and 1500 °C, and the hardness of the SiC bulk is compared with that of other studies.[5,7,10] In the process of HPHT sintering of SiC, the pressure is first increased to 3.8 GPa, then the temperature is increased to 1500 °C, and, finally, the pressure is increased to 5.0 GPa. The hardness of the SiC sinter decreases with increasing loading force and then stabilizes to a final value of 31.3±0.3 GPa. The density of the sample measured by the density balance was 98.4% (±0.3%).

3.2. Process analysis under high pressure and high temperature

3.2.1. Crushing of SiC under high pressing and room temperature

Figure 4 shows the XRD pattern and SEM image of the initial SiC sample powder. In the starting sample, no impure phases or non-stoichiometry were detected through XRD and SEM. The original SiC particles possess a cubic structure and are relatively uniform with good crystalline morphology. Crushing the SiC particles under high pressure is the decisive process of sintering densification of SiC ceramics.

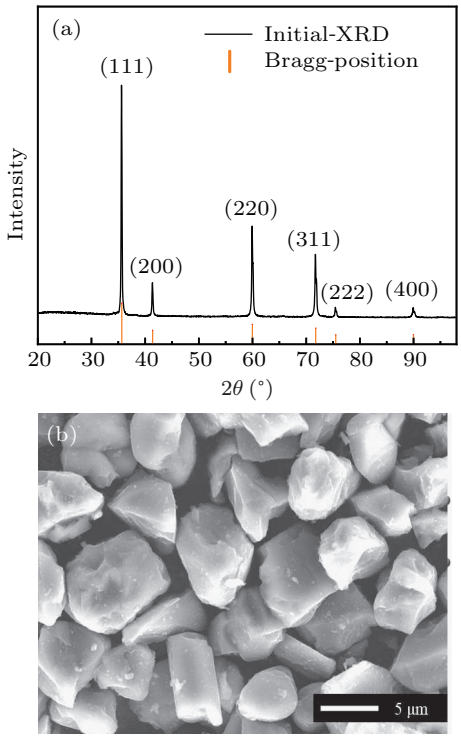


Fig. 4. XRD pattern ($\lambda = 1.5404$ Å) and SEM image of the initial SiC powder in ambient conditions. (a) XRD pattern; (b) SEM image.

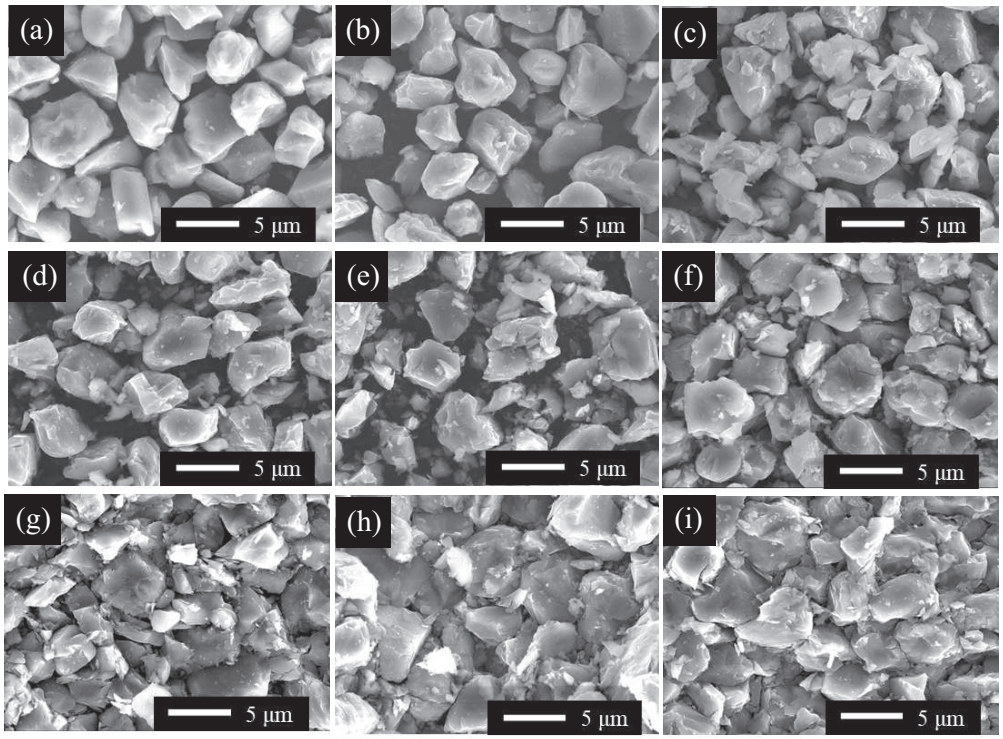


Fig. 5. SEM images of SiC particles crushed under different pressures. (a) Initial powder; (b) 0.5 GPa; (c) 2.3 GPa; (d) 3.8 GPa; (e) 5.0 GPa; (f) 8.5 GPa; (g) 10.0 GPa; (h) 12.0 GPa; (i) 16.0 GPa.

Figure 5 shows the microstructure characteristics of SiC particles under different pressures. SiC has a different fracture morphology under different pressures. In Fig. 5(b), the particle size and morphology are unchanged at 0.5 GPa, and there are no cracks on the surface and edges. In Fig. 5(c), at 2.3 GPa, there are cracks in most corners, and crushing is observed at the edges of the particles first. As crushing intensifies in Fig. 5(d), at 3.8 GPa, large particles become round and regular, and cracks appear in the middle of the particle surface, including parallel and splitting cracks. In Fig. 5(e), the SiC particles are further fragmented at 5.0 GPa, with larger particles surrounded by smaller particles created by fragmentation,

and visible cracks are present on the surface of the large particles. When the pressure is 8.5–16.0 GPa, the particle-crushing process almost stops (Figs. 5(f)–5(i)). The SiC fragments first have cracks on the edges; then the edges and corners fracture, and the grain surface cracks. Even if the pressure continues to increase, each particle is not crushed significantly and there are always large particles present.

3.2.2. Yield strength and stress analysis at room temperature

The yield strength was measured in order to further analyze the mechanism of crushing and refinement of the SiC particles. Figure 6(a) indicates that the structure of SiC is stable in this experimental pressure range. The structural transformation pressure of SiC under cold pressing is very high.[35] The pressure causes the grains to squeeze each other, resulting in microscopic deviatoric stress and the broadening of the diffraction peaks under non-hydrostatic conditions. *In situ* high-pressure synchrotron radiation XRD was used to study the yield strength of materials under high pressure, which was analyzed by the XRD peak width method.[36,37] The microscopic deviatoric strain and grain size dependencies of the diffraction line widths are described by the following equation:[38–40]

$$(2\omega_{hkl}\cos\theta_{hkl})^2 = (\lambda/D)^2 + \eta_{hkl}^2\sin^2\theta_{hkl}, \tag{1}$$

where $2\omega_{hkl}$ represents the FWHM of the diffraction profile on a 2θ scale. The symbols θ_{hkl}, λ, D, and η_{hkl} are the Bragg angle, x-ray wavelength (0.6199 Å), grain size, and microscopic deviatoric strain, respectively. The average grain size and microscopic deviatoric strain distribution can be obtained by plotting $(2\omega_{hkl}\cos\theta_{hkl})^2$ as a function of $(\sin\theta_{hkl})^2$. The microscopic deviatoric strain can be derived from the slope of the straight lines in Eq. (1), and the microscopic deviatoric stress is determined by $\sigma = \eta E$, where E represents the aggregate Young's modulus.[41,42] In Fig. 6(b), the FWHM initially increases with increasing pressure, but the trend begins to flatten out when the pressure reaches 8.5 GPa. In Fig. 6(c), the microscopic deviatoric stress increases linearly with pressure until the pressure reaches 8.5 GPa, and does not change when the pressure exceeds 8.5 GPa. This indicates the beginnings of plastic deformation and the yielding of SiC under high pressure. SiC first undergoes an elastic deformation phase, followed by further compression and strengthening. As a result, SiC has a yield strength of about 8.5 GPa at room temperature, which is consistent with what has been reported in the literature.[43]

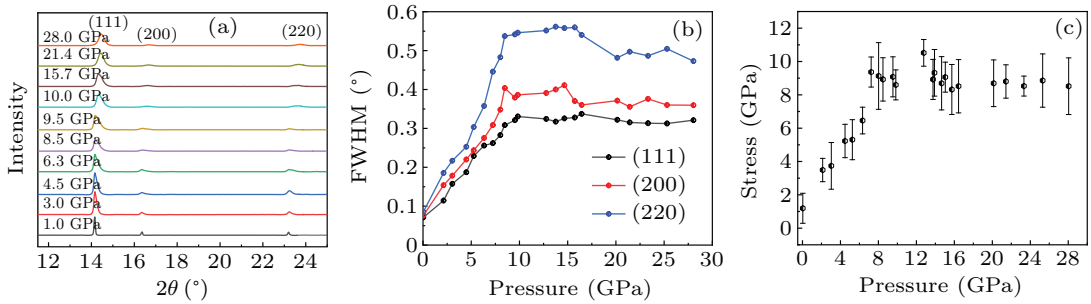


Fig. 6. (a) *In situ* high-pressure synchrotron radiation XRD patterns of SiC samples under various pressures at room temperature (λ = 0.6199 Å). (b) FWHM changes with increasing pressure. (c) Variation of microscopic deviatoric stress with pressure.

A pore exists in the compression of SiC particles, and the stress in the pore is usually lower than in the rest of the grain, resulting in a stress difference between the grains. As shown in Fig. 7(a), there is always a pore between SiC particles in the cold-pressing stage. The stress in the pores is usually lower than in other parts and is referred to as the low-stress area. On the other hand, the stress in the area where particles make contact is higher, and is called the high-stress area. The difference between the high-stress area and low-stress area leads to shear stress, which finally results in the cracking of the SiC grains. The high-stress regions and low-stress regions are determined by the double peak-fitting method and are shown in Fig. 7(b). The (111), (200), and (220) peaks of SiC are deconvoluted into two peaks to obtain the d-spacing representing the low-stress regions and high-stress regions. Then, the relationship between the d-spacing and lattice constant a is

$$d = a/\sqrt{(h^2+k^2+l^2)}. \tag{2}$$

The lattice constant a can be calculated by Eq. (2). Finally, the third-order Birch–Murnaghan equation of state is used to calculate the stress in the high-stress regions and low-stress regions

$$P = 1.5K\left[(V/V_0)^{-7/3} - (V/V_0)^{-5/3}\right] \times\{1+0.75(K'-4)[(V/V_0)^{-2/3}-1]\}, \tag{3}$$

where V represents the unit cell volumes under the external loading pressure of P, V_0 represents the unit cell volumes at ambient conditions, and V/V_0 is the compression ratio of the unit cell volume at each pressure to the unit cell volume under ambient pressure. The value of the SiC bulk modulus (K) is 248 (9) GPa, and its first-order derivative at zero pressure (K') is 3.7 (0.3).[44] Finally, three crystal planes are used to calculate the high-stress regions and low-stress regions.

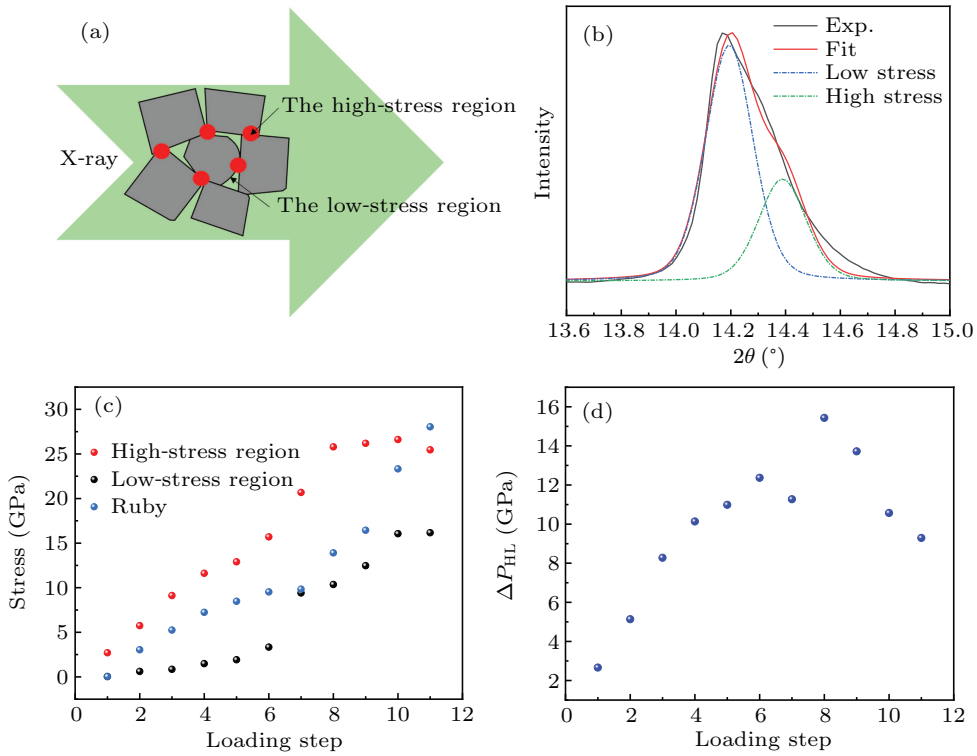


Fig. 7. (a) Schematic diagram of SiC intergranular stress distribution under high pressure. (b) Fitting of the (111) diffraction peak at 8.5 GPa. (c) Stress values for high-stress regions and low-stress regions in SiC grains vs. external loading pressure at different loading steps (the ruby represents the external loading pressure). (d) Difference between the high-stress regions and low-stress regions (ΔP_{HL}) at different loadings.

Figure 7(c) shows the stress values for high-stress regions and low-stress regions in SiC grains and the external loading pressure under different loading steps. Figure 7(d) shows the change of stress difference in the high-stress areas and low-stress areas. The pressure in the low-stress regions increases steadily when the initial external loading is below 8.5 GPa, with a sudden change in pressure at 8.5 GPa. Below 8.5 GPa, the stress difference between the high-stress zones and low-stress zones increases with increasing external loading pressure. When it exceeds 8.5 GPa, the stress difference in the high-stress zones and low-stress zones gradually decreases with the external loading pressure, resulting in SiC particles no longer crushing. It is worth noting that the yield strength of the SiC sample is precisely when the pressure in the low-stress region changes abruptly. This phenomenon demonstrates that there are different forms of contact and voids between particles before the load pressure of the SiC powder reaches the yield strength, which results in the reduction of stress in the gap between particles. After the load pressure reaches the yield strength, it undergoes a short plastic stage and then breaks, which increases the stress of the grains in the gap and makes the low-stress area more sensitive, resulting in the stress changing first in the low-stress area. The overall stress state and local stress in grains change with the expansion of contact between grains.

3.2.3. Defect structure analysis

Different particle morphologies and internal defects lead to different forms of fracture. Figure 8 shows the surface cracks and internal microdefects of the particles. The SiC particles show elastic behavior under cold pressing, producing distinct brittle fracture cracks. The grain microdefects first appear during cold pressing. In the SiC grains, the dislocation density increases with increasing pressure. A further increase in pressure results in the dislocation slip band failing to move, which is usually accompanied by the development of submicron microcracks. Then, from within the grain, the cracks extend to the grain surface, causing severe cracking that eventually fractures at the grain boundaries. The cracking and fracture will occur first at the corners during cold pressing due to the high-defect density observed in the grain contact area.

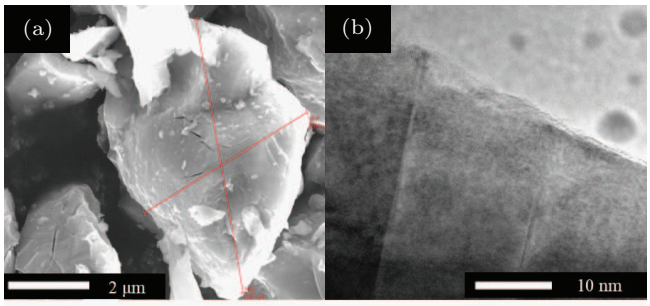


Fig. 8. (a) Crack on particle surfaces under 5.0 GPa cold pressing. (b) TEM characterization of cold-pressed SiC samples at 5.0 GPa.

Figure 9 shows many microdefects within the sintered SiC synthesized at 1100 °C and 5.0 GPa, such as dislocation accumulations, intersecting microtwins, and stacking faults. These microtwin defects can make SiC produce higher hardness.[45] There are more microdefects compared to cold

pressing, indicating that more defects can be produced at low temperatures. For the isothermal-compression process, increasing the pressure while keeping the temperature constant can create more defect structures. Some defects are already generated during the cold-pressing process, and the defects are then further increased during the low-temperature process. Temperature further promotes the deformation of the grains to generate more defects.[46] Compared with the traditional experiment of increasing the pressure first and then the temperature, our isothermal-compression process is to increase the pressure while the temperature is unchanged. The higher the temperature, the lower the yield strength of the material. At a constant temperature during the isothermal-compression process, a further increase in pressure will produce dynamic plastic deformation of the SiC and a large number of defects will occur; finally, the hardness will be improved. Therefore, the sintering quality of SiC samples can be significantly improved by the HPHT sintering method, which finally leads to an increase in the hardness of SiC.

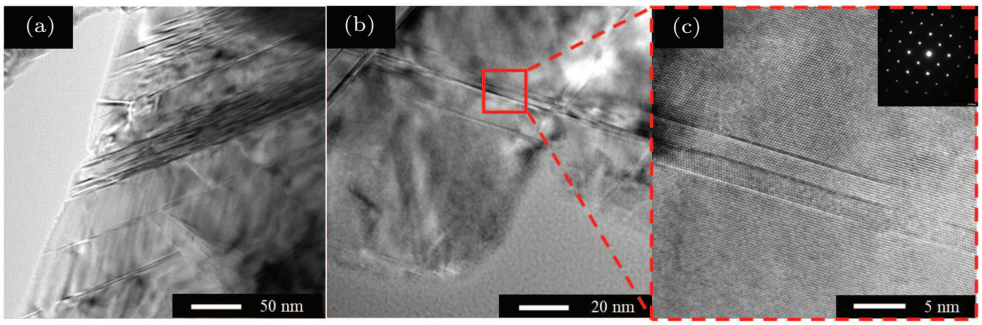


Fig. 9. TEM characterization of SiC samples sintered at 5.0 GPa and 1100 °C. (a) Defect structure of the sample surface; (b) intersecting microtwins; (c) nanotwin boundaries in the defect section.

4. Conclusions

In conclusion, the HPHT sintering of SiC micron particles was studied. Pure phase micron SiC bulk material with a hardness of 31.3±0.3 GPa was successfully sintered by isothermal-compression methods. The sample had a density of 98.4% (±0.3%). SiC grains developed microscopic defect structures during cold pressing. Defects such as dislocations were unable to slide under pressure and this led to the development of submicron microcracks. SiC grains exhibited high- and low-stress regions, with higher stress in the grain-contact regions, resulting in the crushing of SiC particles, which showed fractures at the edges and corners, as well as the cracking of crystal planes as the pressure increased. During the sintering process, the surface cracks in the particles first closed, then grain boundary creep occurred. Subsequently, plastic deformation under the influence of temperature occurred, followed by densification. Therefore, during HPHT sintering, it is possible for isothermal-compression processes to produce SiC materials of higher hardness by first increasing the pressure to produce crushing and defects in the SiC, then by increasing the temperature to produce plasticity, and lastly by maintaining the temperature while increasing the pressure to the desired pressure to produce more defects. This research provides a new perspective for the preparation of pure-phase bulk materials with superior properties.

Acknowledgements

Project supported by the National Natural Science Foundation of China (Grant No. 12074273). High-pressure synchrotron radiation XRD experiments were carried out at the 4W2 beamline of the Beijing Synchrotron Radiation Facility (BSRF).

References

[1] Guo X Z, Yang H, Zhang L J and Zhu X Y 2010 *Ceram. Int.* **36** 161
[2] Tanaka H 2002 *J. Ceram. Soc. Jpn.* **110** 877
[3] Casady J B and Johnson R W 1996 *Solid State Electron.* **39** 1409
[4] Liao Q, Li B S, Kang L and Li X G 2020 *Chin. Phys. B* **29** 076103
[5] Rahman A, Singh A, Harimkar S P and Singh R P 2014 *Ceram. Int.* **40** 12081
[6] Feng D, Ren Q X, Ru H Q, Wang W, Jiang Y, Ren S Y and Zhang C P 2019 *Ceram. Int.* **45** 23984
[7] Barick P, Chakravarty D, Saha B P, Mitra R and Joshi S V 2016 *Ceram. Int.* **42** 3836
[8] Zhao Y C and Wang M Z 2007 *Chin. Phys. Lett.* **24** 2412
[9] Li Y D, Cheng Y S, Su M J, Ran Q F, Wang C X, Ma H A, Fang C and Chen L C 2020 *Chin. Phys. B* **29** 078101
[10] Sun R X, Wei X D, Hu W T, Ying P, Wu Y J, Wang L Y, Chen S, Zhang X, Ma M D, Yu D L, Wang L, Gao G Y, Xu B and Tian Y J 2022 *Small* **18** 2201212
[11] Matovic B, Zivic F, Mitrovic S, Prsic D, Maksimovic V, Volkov-Husovic T, Kumar R and Daneu N 2016 *Mater. Lett.* **164** 68
[12] Guan S X, Peng F, Liang H, Fan C, Tan L J, Wang Z W, Zhang Y F, Zhang J W, Yu H and He D W 2018 *J. Appl. Phys.* **124** 215902
[13] Xiang X J, Song G Z, Zhou X F, Liang H, Xu Y, Qin S J, Wang J P, Hong F, Dai J H, Zhou B W, Liang W J, Yin Y Y, Zhao Y S, Peng F, Yu X H and Wang S M 2020 *Chin. Phys. B* **29** 088202
[14] Matović B, Bučevac D, Urbanović V, Stanković N, Daneu N, Volkov-Husović T and Babic B 2016 *J. Eur. Ceram. Soc.* **36** 3005
[15] Bobrovnitchii G S, Osipov O S and Filgueira M 2003 *Int. J. Refract. Met. H* **21** 251
[16] Xiong Z B, He D X, Peng F, Guan S X, Tan L J, Yu H, Xiang X J and Liang H 2020 *Int. J. Refract. Met. H.* **92** 105311
[17] Xie H, Deng F M, Yang X F and Han S L 2020 *Ceram. Int.* **46** 1631
[18] Deng F M, Yang X F, Deng W L, Zhou L L, Wang H and Zhang Z W 2019 *Diam. Relat. Mater.* **96** 25
[19] Daouadji A, Hicher P Y and Rahma A 2001 *Eur. J. Mech. A-Solid* **20** 113

[20] Su Y Z, Wang J P, Li X, Tang Q Q, Yang J, Lei L, Tian Y, Wang Z W and He D W 2021 *Ceram. Int.* **47** 21077
[21] Gruzdeva E N, Kardasevich V S, Suranov A V, Nesterenko T N and Rotner Y M 1985 *Sov. Powder Metall. Met. Ceram.* **24** 603
[22] Li R R, Zhang Y F, Geng D C, Zhang G W, Watanabe H, Han W T and Wan F R 2019 *Acta Phys. Sin.* **68** 216101 (in Chinese)
[23] Sun J F, Li X P, Liang B Y, Zhao Y C and Wang M Z 2009 *Chin. Phys. Lett.* **26** 078102
[24] Britun V F, Oleynik G S and Semenenko N P 1992 *J. Mater. Sci.* **27** 4472
[25] Casanova C A M, Balzaretti N M, Voronin G and da Jornada J A H 1999 *Diam. Relat. Mater.* **8** 1451
[26] Moller H J and Welsch G 1985 *J. Am. Ceram. Soc.* **68** 320
[27] Yu X H, Raterron P, Zhang J Z, Lin Z J, Wang L P and Zhao Y S 2012 *Sci. Rep.* **2** 876
[28] Lu J R, Kou Z L, Liu T, Yan X Z, Liu F M, Ding W, Zhang Q, Zhang L L, Liu J and He D W 2017 *Diam. Relat. Mater.* **77** 41
[29] Weidner D J, Wang Y B and Vaughan M T 1994 *Science* **266** 419
[30] Peng B, Kou Z L, Zhao M X, Jiang M L, Zhang J W, Wang Y P and Zhang L 2020 *Chin. Phys. B* **29** 090703
[31] Daviau K and Lee K K M 2017 *Phys. Rev. B* **95** 134108
[32] Kidokoro Y, Umemoto K, Hirose K and Ohishi Y 2017 *Am. Mineral.* **102** 2230
[33] Liang H, Guan S X, Li X, Liang A K, Zeng Y, Liu C Q, Chen H H, Lin W T, He D W, Wang L P and Peng F 2019 *Ceram. Int.* **45** 7885
[34] Weidner D J, Wang Y B and Vaughan M T 1994 *Geophys. Res. Lett.* **21** 753
[35] Yoshida M, Onodera A, Ueno M, Takemura K and Shimomura O 1993 *Phys. Rev. B* **48** 10587
[36] Yu H, Peng F, Liang H, Guan S X, Tan L J, Xiong Z B, Xiang X J, Li Q Z, Lei L and He D W 2019 *J. Phys. Chem. C* **123** 28437
[37] Chen H H, Liang H, Peng F, Li H S, Wang B, Xia X X, Li X D, Wang P and Wang L P 2019 *Inorg. Chem.* **58** 405
[38] Singh A K, Liermann H-P, Akahama Y and Kawamura H 2007 *J. Appl. Phys.* **101** 123526
[39] He D W and Duffy T S 2006 *Phys. Rev. B* **73** 134106
[40] Liang H, Chen H H, Peng F, Liu L X, Li X, Liu K, Liu C Q and Li X D 2018 *J. Phys. Chem. Solids* **121** 256
[41] Tan J, Meadows P J, Zhang D, Chen X, López-Honorato E, Zhao X, Yang F, Abram T and Xiao P 2009 *J. Nucl. Mate.* **393** 22
[42] Lambrecht W R L, Segall B, Methfessel M and van Schilfgaarde M 1991 *Phys. Rev. B* **44** 3685
[43] Demetriou M D, Launey M E, Garrett G, Schramm J P, Hofmann D C, Johnson W L and Ritchie R O 2011 *Nat. Mater.* **10** 123
[44] Strossner K, Cardona M and Choyke W J 1987 *Solid State Commun.* **63** 113
[45] Lin Z J, Wang L, Zhang J Z, Guo X Y, Yang W G, Mao H K and Zhao Y S 2010 *Scr. Mater.* **63** 981
[46] Hao G L, Wang X F and Li X Y 2015 *Chin. Phys. Lett.* **32** 026103